Nuclear Materials and Energy 15 (2018) 115–121

Contents lists available at ScienceDirect

Nuclear Materials and Energy

journal homepage: www.elsevier.com/locate/nme

Cavity evolution and hardness changes in a 15Cr-ODS ferritic steel by post He-implantation annealing

Peng Song[a,*], Kiyohiro Yabuuchi[b], Akihiko Kimura[b]

[a] Graduate School of Energy Science, Kyoto University, Yoshida-honmachi, Sakyou-ku, Kyoto 606-8501, Japan
[b] Institute of Advanced Energy, Kyoto University, Gokasho, Uji, Kyoto 611-0011, Japan

ARTICLE INFO

Keywords:
Cavity evolution
Nanoindentation hardness
ODS steel
He implantation
Annealing

ABSTRACT

15Cr-ODS ferritic steel was implanted with 3500 appm He (0.2 dpa) at 300, 550 and 700 °C. The post-implantation annealing (PIA) at 800 °C/100 h was conducted on the specimen implanted at 300 °C. Nanoindentation (NI) tests were carried out to investigate the temperature dependent hardening, and transmission electron microscopy (TEM) observation was performed to characterize the cavity evolution. A limited hardening was found in the as-implanted ODS specimens at all implantation temperatures, which tended to reduce with increasing the temperature. The PIA caused no further hardening, while TEM images revealed that there was an evident change in the cavity distribution morphology. The cavity diameter increased from 2.5 ± 0.4 nm to 5.0 ± 1.7 nm and the corresponding number density decreased from (22.2 ± 1.6) × 10^{22} m^{-3} to (6.7 ± 0.5) × 10^{22} m^{-3} before and after the PIA. The negligible hardness changes induced by the PIA were interpreted in terms of the Orowan-type dislocation barrier model with the corresponding barrier strength factor of cavities to be less than 0.1.

1. Introduction

Oxide dispersion strengthened (ODS) steels have been considered as a candidate structural material of first wall/blanket for future fusion reactors because of their outstanding mechanical properties, especially high-temperature strength [1,2], and acceptable corrosion resistance against coolants [1], as well as excellent radiation tolerance such as low swelling and hardening [2,3]. In the fusion structural material, numerous helium (He) atoms are produced by (n, α) nuclear reactions. Moreover, the formation of He-Vacancy (He-V) clusters, involving nanosized He bubbles, cavities and large voids, may lead to swelling, hardening, embrittlement and reduction in creep properties [4].

In the conventional ferritic/martensitic (F/M) steels, He-induced hardening is still a matter of discussion. Jung et al. investigated the effect of the implanted He on tensile properties of 9Cr-martensitic steels (EM10 and T91) using an ion accelerator at temperatures from 150 °C to 550 °C with He concentrations between 1250 and 5000 appm at 0.2 and 0.8 dpa, respectively [5]. Based on the dependence of irradiation hardening on He concentration and dpa, they attributed the hardening to He bubbles without TEM examinations [5]. Henry et al. [6] performed TEM examinations and SANS analysis for the same steels as those in Ref. [5] implanted with 5000 appm He. Indeed, they concluded again that the evident hardening was attributed to He bubbles at the implantation temperatures between 250 and 550 °C, although no He bubbles but dot shaped small defect clusters, probably dislocation loops, were observed by TEM in the steel implanted with 5000 ppm He at 250 °C. Additionally, they mentioned that the barrier hardening model with a strength factor of 0.4 gave an insufficient hardening by small defect clusters. Farrell et al. [7] compared the tensile properties of F/M steels irradiated in HFIR and LANSCE spanning the dose range 0.01–24 dpa up to about 1000 appm He. As a result, there was no sign of a large hardening contribution attributable to the presence of He at the irradiation temperatures below 160 °C. Furthermore, Henry et al. [8] reported on tensile properties of 9Cr-1Mo (EM10) tempered martensitic steel irradiated in spallation conditions (133–301 °C, 4–11 dpa, 150–890 appm He, 1270–4800 appm H) and after the irradiation with fission neutrons in OSIRIS reactor (325 °C, ~1–9.3 dpa) that the amount of irradiation hardening showed a similar trend of dose dependence. Dai et al. [9] investigated the dpa dependence of irradiation hardening of T91 irradiated at below 300 °C in SINQ Target-3, and reported that the dpa dependence of hardening was changed over 5.9 dpa (He = 390 appm) above which He bubbles contributed to an additional hardening. More recently, Dai et al. reported that an evident hardening (ΔHV = ~80 kg/mm^2) was left in the post-irradiation annealed (600 °C/2 h) F/M steels after the irradiation in SINQ (1175 appm/11.3 dpa), which was attributed to the contribution of He

* Corresponding author.
E-mail address: p-song@iae.kyoto-u.ac.jp (P. Song).

https://doi.org/10.1016/j.nme.2018.03.006
Received 9 January 2018; Received in revised form 11 March 2018; Accepted 12 March 2018
Available online 21 March 2018

bubbles [10].

As for the ODS F/M steels, the ODS F/M steel with He ion implantation (3360 appm/0.84 dpa) also presented a temperature dependent hardening behavior: declining from ~15% at 100 °C to ~3.5% at 500 °C [11], which might be accompanied by cavity evolution [12]. Nevertheless, some discrepancies still exist for the He induced hardening in ODS F/M steels. Roldán et al. reported that the implantation of about 750 appm He brought about a 21% hardening in Eurofer ODS at 70 °C [13], while at 30 °C/9 at.% He/3 dpa, a 31% hardening was produced in the same ODS steel [14]. At such low temperatures, it is difficult to separate the pure hardening contribution of He bubbles from those of fine defect clusters or dislocation loops.

Post-implantation annealing (PIA) may be an effective way to distinguish the contributions of dislocation loops and He-V clusters, and possibly lead to an assessment of the pure bubble hardening. In a 14Cr-YWTi nanostructured ferritic alloy with 12–14 at.% He implantation at 400 °C, the mean cavity size increased from 2.2 nm in the as-implanted case to 2.7 nm after the PIA at 750 °C/100 h [15]. The corresponding number densities of cavities increased from $\sim 8 \times 10^{23}$ m^{-3} to $\sim 12 \times 10^{23}$ m^{-3} after the PIA [16]. Nevertheless, hardening was not addressed in those works [15,16].

Therefore, in this study, at first, we aimed to investigate the effect of high concentration He implantation at various temperatures. Second, the post-implantation annealing behavior of NI hardness and the microstructure evolution process were examined to assess the contribution of cavities to the hardening.

2. Material and methods

The material used in this study was a 15Cr-ODS ferritic steel which was produced by mechanical alloy processing, followed by hot extrusion and forging at 1150 °C. The final heat treatment was an annealing at 1150 °C for 1 h followed by air-cooling. The resultant compositions (wt.%) were Fe-14.59Cr-1.84W-0.14Ti-3.46Al-0.27Zr-0.33Y_2O_3. The averaged grain size of the studied ODS steel was estimated to be about 370 nm based on electron backscatter diffraction (EBSD) measurements [12].

Specimens were sampled so that the specimen surface was perpendicular to the extrusion direction. The specimen surface was mechanically polished and then electrolytic polishing was conducted in a solution of 10% (vol.) $HClO_4$ and 90% (vol.) CH_3COOH at room temperature. Specimens were irradiated with 1 MeV He^+ at the DuET facility in Kyoto University [17]. The beams were by the raster scan at a frequency of 1000 Hz in a horizontal direction and 300 Hz in a vertical direction. He^+ beam was inclined with 45° to the normal of the specimen surface and a rotating energy degrader foil was applied for obtaining a rather homogenous distribution of helium atoms in the specimens. The averaged flux of He^+ ions was 1.7×10^{16} ions m^{-2} s^{-1}. The irradiation temperature was measured by an infrared thermography to be 300, 550 and 700 °C with in a fluctuation of ± 10 °C. The injected helium concentration and displacement damage (displacements per atom, dpa) were obtained by SRIM [18] simulation with use of the Kinchin-Pease method (shown in Fig. 1), recommended by Stoller et al. [19]. At the region 1000–1300 nm from the specimen surface, the He concentration was about 3500 appm and the corresponding damage level was approximately 0.2 dpa.

Specimens as implanted at 300 °C, which were placed in one evacuated quartz tube with Zr thin films for mitigating the surface oxidation of the specimens, were annealed at 800 °C for 100 h in a vacuum of 6×10^{-3} Pa followed by furnace-cooling. In order to eliminate the effect of aging itself, as-received specimens were also aged at 800 °C for 100 h and compared with those He-implanted specimens.

Cross-sectional transmission electron microscopy (TEM) specimens were fabricated by the lift-out technique using a Focused Ion Beam (FIB). Prior to TEM observations, flash polishing was done by using a solution of 5% (vol.) $HClO_4$ and 95% (vol.) CH_3OH at approximately −35 °C for the removal of FIB damage layer. Subsequently, the microstructure was observed by using a conventional 200 kV JEOL JEM 2010 microscope. Further, cavities were imaged by the Fresnel contrast and the cavity size was carefully measured one by one according to the edge dark fringe (under-focus) or bright fringe (over-focus) of cavities. More details were described in the Ref. [12].

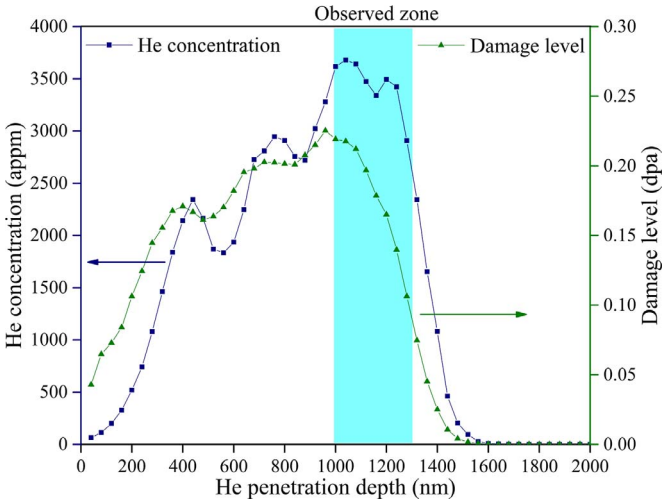

Fig. 1. He concentration (appm) and damage level (dpa) of a Fe-15Cr alloy as a function of the He-ion penetration depth, as predicted by SRIM simulation (He implanted to a fluence of 4.5×10^{20} He m^{-2}).

Nanoindentation (NI) tests were carried out by using a nanoindenter (Agilent G200) equipped with a Berkovich tip at 20 °C. Continuous stiffness measurement (CSM) was adopted to obtain the profiles of continuous hardness and elastic modulus versus indentation displacement. Before testing, the indenter tip geometry was calibrated by indenting a standard material fused silica. Key testing parameters were as follows: the strain rate was 0.05 s^{-1}, the harmonic displacement was 1 nm and the testing Poisson's ratio of ODS samples was 0.3. For each specimen, 24 testing points (50 μm between two adjacent points) were chosen and the averaged hardness was obtained by calculating the measured hardness data of roughly 20 tests.

3. Results and discussion

3.1. He-ion implantation hardening

The depth profiles of the averaged nanoindentation hardness (H_{NI}) for the as-received and as-implanted specimens are shown in Fig. 2(a), indicating that the averaged H_{NI} continuously decreased with increasing the indentation depth (h) from roughly 50 nm to 1500 nm, which is known as the indentation size effect (ISE) [20]. In order to evaluate irradiation hardening, we needed to choose an adequate depth that reflects microstructural changes by ion implantation. The hardness in the near surface depth region, which is shallower than 200 nm, is strongly affected by the depth because of the ISE, whereas in the region deeper than 300 nm, the hardness may already be influenced by unirradiated region since the depth of the plastic deformation region created by a nanoindent is approximately five times or more of the indentation depth [21–24]. Therefore, we selected the indentation depth of 250 nm as a reference H_{NI} to evaluate He-implantation hardening [23,24]. All the depth profiles in Fig. 2(a) show the similar trend. The profiles of He-implanted specimens at 300 and 550 °C are located at the upper side but that at 700 °C is at the lower side of as-received specimen, although the differences are within an error bar.

Nix and Gao developed a model to evaluate a bulk relevant macrohardness for a surface thin layer based on the concept of geometrically necessary dislocations [20], which is described in the following

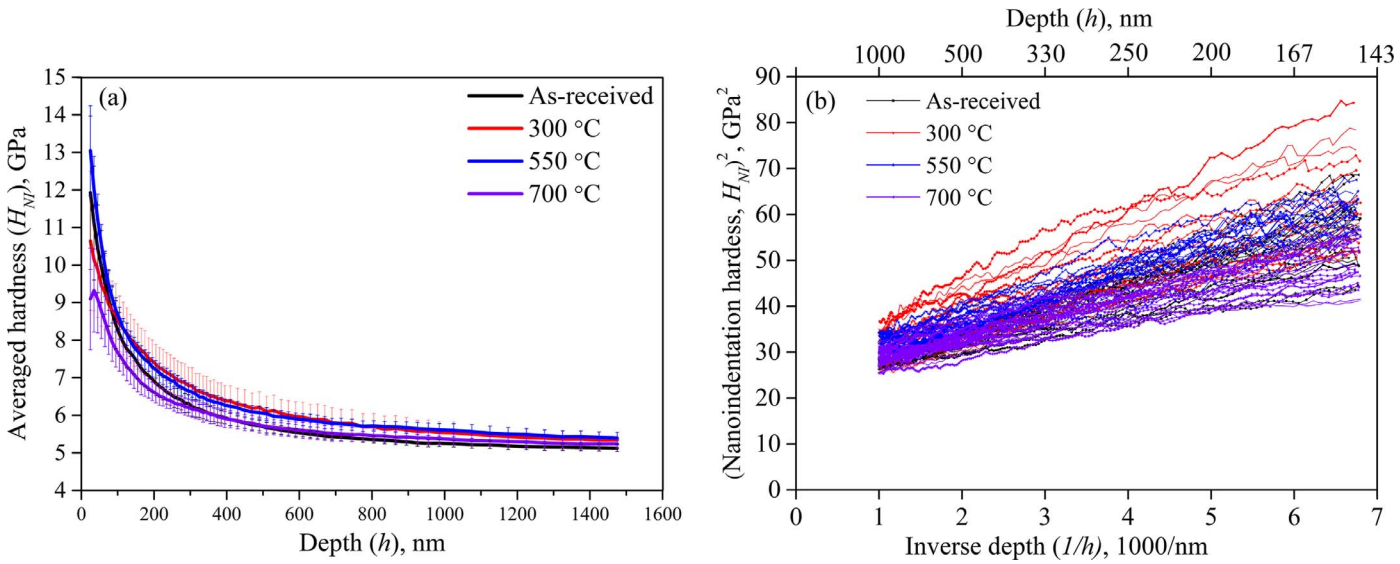

Fig. 2. (a) Depth profiles of the average hardness (H_{NI}) for the as-received specimen and as-implanted ones at 300, 550, 700 °C; and (b) plots of square nanoindentation hardness $(H_{NI})^2$ versus the reciprocal indentation depth ($1/h$). (color figure).

equation that explains the depth dependence of hardness:

$$H/H_0 = \sqrt{(1 + (h^*/h))} \quad (1)$$

where H is the hardness at a certain indentation depth, h, and H_0 is the hardness in the limit of infinite depth that is defined to be the bulk relevant hardness. h^* is a characteristic length that depends on the indenter shape, H_0 and the shear modulus, but is not a constant for a given material and indenter geometry. It is a function of the density of statistically stored dislocations via H_0. Ideally plotting the square of the hardness against the reciprocal of the indentation depth should deserve a straight line, the intercept and the slope of which are the square of H_0 and h^*, respectively [20]. Fig. 2(b) shows the corresponding plots of square nanoindentation hardness $(H_{NI})^2$ versus the reciprocal indentation depth ($1/h$), where all the tangent lines in the indentation depth range of 150–1000 nm and 150–250 nm were used to evaluate the H_{NI} for the as-received and the as-implanted specimen, respectively. Thus, the averaged H_0 values were obtained, being the bulk relevant hardness of an un-implanted layer or a He-implanted layer.

All the measured hardness values and the hardness changes are shown in Fig. 3 and the numerical values are presented in Table 1. The hardness changes were generally similar for those obtained by the two methods. Fig. 3(a) and 3(c) showed that a small hardening was induced by He-ion implantation and gradually declined with increasing the implantation temperature. At 300 °C, the hardness changes at approximately 250 nm and obtained by the Nix-Gao model were 514 ± 582 MPa and 544 ± 417 MPa, respectively. Such rather large errors in the hardness changes come from the errors in the obtained hardness values before and after implantation where the latter were less than 8%. In this study, the effect of He-ion implantation on hardness was small, which made errors appear to be large. Therefore, we think the current experimental results are still meaningful for a discussion of the implantation effect.

Temperature dependent microstructural evolution under the He-ion implantations has been discussed in Ref. [12], which revealed that He bubbles grew up with decreasing number density as the temperature went up from 300 °C to 700 °C.

3.2. Cavity evolution during PIA treatment

After the implantation at 300 °C, up to 3500 appm He/0.2 dpa (about 1000–1300 nm), almost no dislocation loops were observed, except for spherical tiny He bubbles with the mean diameter and the

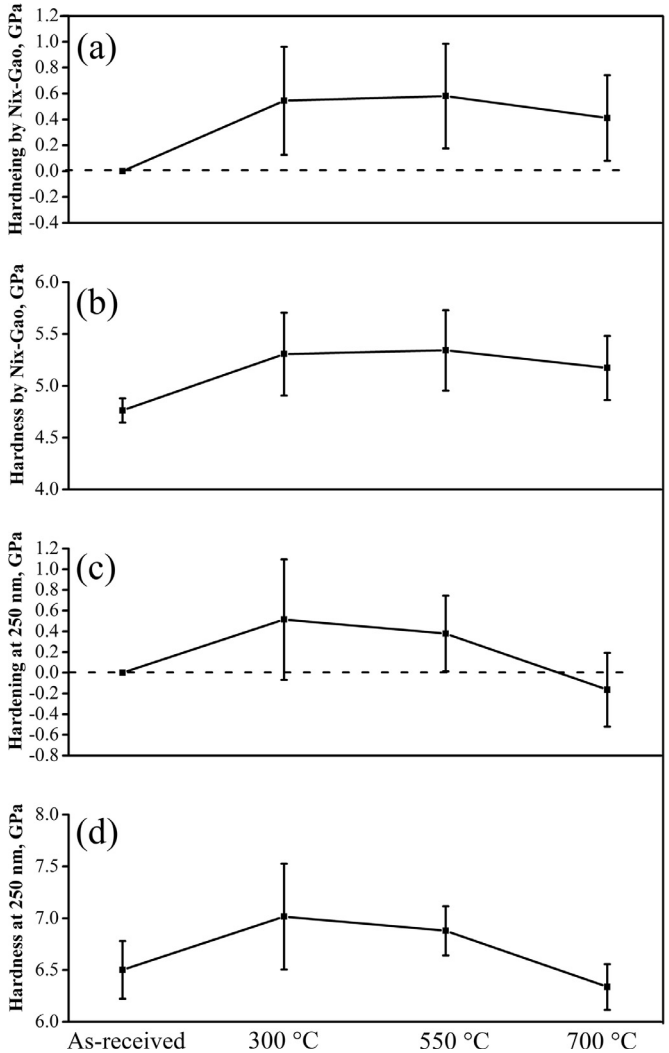

Fig. 3. Nanoindentation hardness (b, d), hardening (a, c) at an indentation depth of 250 nm and obtained by the Nix-Gao plotting for the as-received and as-implanted specimens at 300, 550 and 700 °C.

Table 1
Summary of the measured hardness (ΔH_{NI}, MPa) for each implantation condition and the estimated barrier strength factors of cavities (α_c) based on the TEM examinations.

		As-implanted at 300 °C	As-implanted at 550 °C	As-implanted at 700 °C	PIA at 800 °C/100 h
At 250 nm	ΔH_{NI}	514 ± 582	377 ± 365	− 164 ± 355	4 ± 410
	α_c	0.085	0.0912	–	0.00085
Nix-Gao model	ΔH_{NI}	544 ± 417	580 ± 405	410 ± 331	− 116 ± 294
	α_c	0.09	0.14	0.083	–

"–" means no valid estimated α_c values.

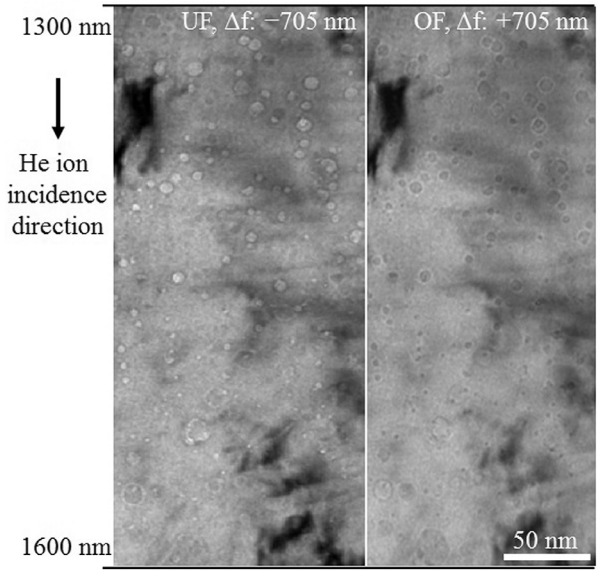

Fig. 4. Cavities in the depth range of approximately 1300–1600 nm from the implanted surface imaged at under-focus (UF) (left) and over-focus (OF) (right) conditions after PIA at 800 °C/100 h.

number density of 2.5 ± 0.4 nm and (22.2 ± 1.6) × 10^{22} m^{-3}, respectively. After the PIA at 800 °C/100 h, a similar microstructure in the end of He implantation range was observed as shown in Fig. 4, where the cavities were imaged at under-focus (left) and over-focus (right) conditions. The He ion implantation direction is from top to bottom. The spots, changing from white at under-focus to dark at over-focus due to the Fresnel contrast, were considered to be He-cavities. What's more, the cavities became sparser and smaller with increasing depth, in accordance with the He concentration profile predicted by the SRIM simulation. Fig. 5(a) depicts an inhomogeneous distribution of cavities in the depth range of ~1000–1300 nm in the PIA specimen. The dashed rectangle region is enlarged in Fig. 5(b), where round, irregular and "crescent moon" shaped cavities existed. The "crescent moon" cavities, pointed out with black arrows but not observed before annealing, were probably attached with the surface of large oxides in the ODS steel, also being observed in another research [25]. After PIA, the number density and the average diameter of cavities were 5.0 ± 1.7 nm and (6.7 ± 0.5) × 10^{22} m^{-3}, respectively. The other parameters of cavities are presented in Table 2.

Fig. 6 shows the statistical size distribution for all the cavities (Fig. 6(a)), cavities in ferrite matrix (Fig. 6(b)), cavities at grain boundaries (GBs) and sub-GBs (Fig. 6(c)) before and after the PIA. For the as-implanted at 300 °C, the size distribution of spheroidal He bubbles was narrow irrespective of their nucleation sites. Following the PIA at 800 °C/100 h, all the cavity size distributions became much broader. Additionally, the minimum and maximum cavity sizes were

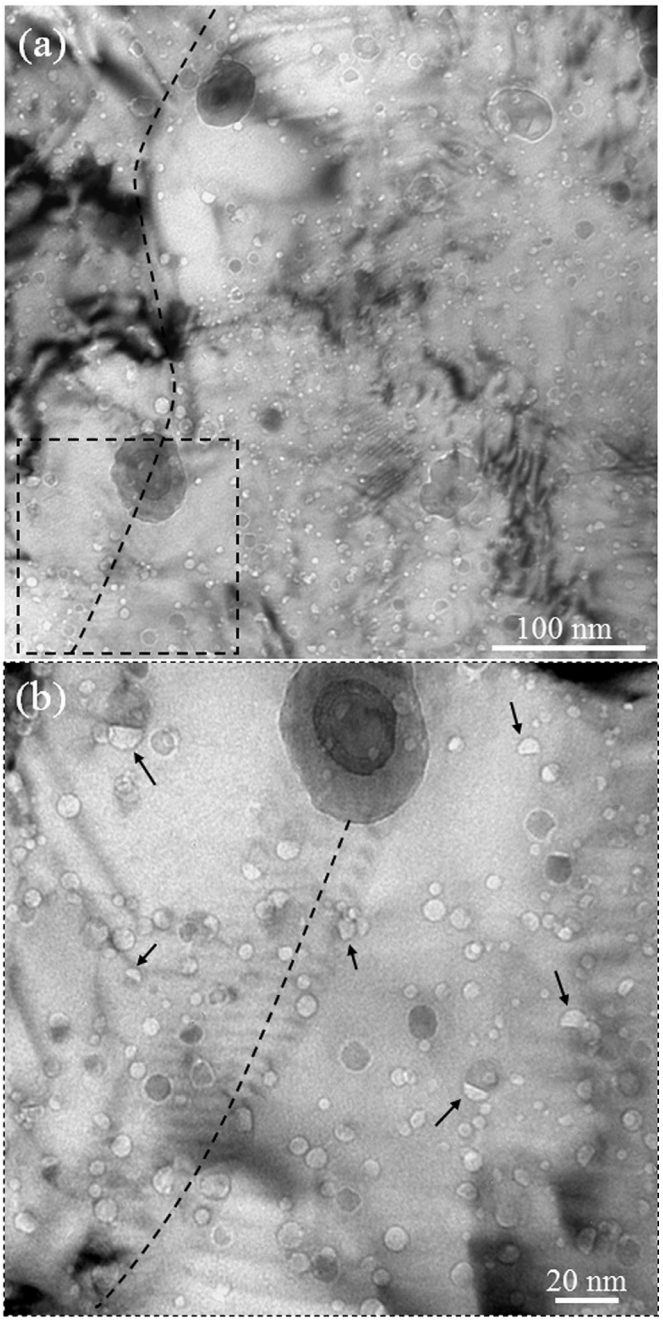

Fig. 5. (a) Cavities in the depth range of about 1000–1300 nm from the implanted surface after PIA at 800 °C/100 h. (b) Enlarged image of dashed rectangle in Fig. 5(a). Arrows mark "crescent moon" resembling cavities.

Table 2
The average diameter (d_c, nm), standard deviation (St. Dev., nm), minimum (Min., nm) and maximum diameters (Max., nm), number density (N_c, × 10^{22} m^{-3}), number (T) of cavities counted in the specimens implanted with He at 300 °C before and after PIA.

	As-implanted at 300 °C			PIA at 800 °C/100 h		
	All cavities	Matrix	GBs	All cavities	Matrix	GBs
d_c	2.51	2.53	2.44	5.03	4.89	6.23
St. Dev.	0.38	0.37	0.40	1.66	1.57	1.94
Min.	1.68	1.68	1.71	1.85	1.85	3.08
Max.	3.79	3.79	3.23	10.95	9.34	10.95
N_c	22.2 ± 1.6 [12]			6.7 ± 0.5		
T	379	325	54	306	274	32

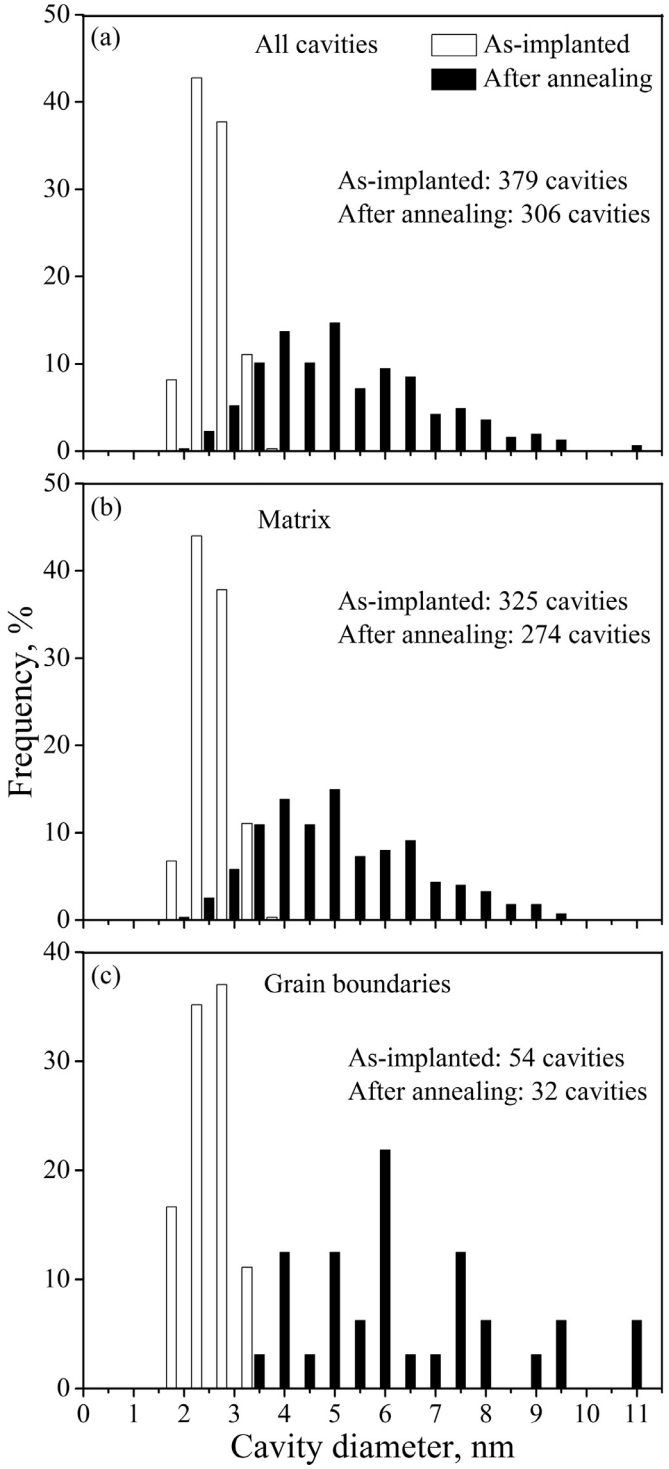

Fig. 6. Size distributions for all the cavities (a), cavities in the ferrite matrix (b) and cavities at the grain boundaries (c) in the specimens implanted with He at 300 °C before and after thermally aging at 800 °C/100 h in the depth range of roughly 1000–1300 nm (3500 appm He/0.2 dpa).

1.85 and 10.95 nm, respectively, while the minimum size in the ferrite matrix was close to the counterpart of 1.68 nm in the as-implanted case before the thermal aging. Edmondson et al. ascribed the cavity coarsening to the punching out of self-interstitial and dislocation loop, Brownian motion and coalescence and Ostwald ripening [15]. Actually, in this study He bubbles grew up to large cavities under the thermal aging at 800 °C/100 h, where the large cavities might be agglomerations of vacancies, of which the internal gas pressure should be far smaller than the surface tension. Despite that, it is difficult to define the characteristics of cavities during PIA by the hard sphere equation of state (HSEOS) [26] without He atom concentration in the cavities.

The nucleation sites of cavities were examined. In the depth range of 1000–1300 nm, microstructures were observed by using $\boldsymbol{g} = [1\bar{1}0]$ close to zone [111] with $\boldsymbol{s}_{\boldsymbol{g}} \neq 0$ under kinematical bright field (KBF) imaging conditions, as shown in Fig. 7. At an in-focus condition, oxide particles and precipitates were imaged as dark spots of the strain contrast as shown in Fig. 7(b), while at defocusing conditions of under-focus or over-focus, cavities were imaged as bright dots (see Fig. 7(a)) or dark dots (see Fig. 7(c)) of the Fresnel contrast as mentioned before. It appears that numerous cavities were attached to dislocations, oxide particles and precipitates, as shown in the two magnified pictures on the left end of Fig. 7. However, it is difficult to accurately figure out the corresponding cavity fractions trapped at dislocations on the basis of $\boldsymbol{g}\cdot\boldsymbol{b}$ invisibility criterion of dislocations with the two-dimensional observations. In the 14Cr-YWT nanostructured ferritic alloy [16], atom probe tomography results showed that 44% of nano-oxide clusters had He bubbles associated with them after the PIA at 750 °C/100 h. Besides, as marked by the dashed curves in Fig. 5(a), few cavities were detected along GBs and sub-GBs, probably owing to the weaker vacancy/helium sink strength of GBs and sub-GBs than the sum of dislocations, oxide particles and precipitates in the ferrite matrix [2], suggesting a good resistance to He induced GB embrittlement in the studied ODS ferritic steel.

3.3. Hardness change by PIA treatment

After the PIA treatment at 800 °C/100 h, the averaged hardness (H_{NI}) versus the indentation depth (h) profile was almost identical to those of the un-implanted specimens before and after the thermal aging. Comparing the PIA treated specimen with the un-implanted being thermally aged, the hardness changes were estimated to be 4 ± 410 MPa and − 116 ± 294 MPa based on the nanoindentation hardness values at around 250 nm and those obtained by the Nix-Gao model, respectively (see Table 1). No matter how much hardening contributed by He-Vacancy clusters, the pure hardening produced by cavities should be negligible for the PIA case. Changes of the hardness between the as-implanted at 300 °C and the PIA treated are compared as shown in Fig. 8. It turned out that the limited hardening produced by He-implantation was further eliminated by the PIA.

3.4. Temperature dependent hardening mechanisms

In general, the He ion implantation hardening was observed at low temperatures below 250 °C in the F/M steels [5,6] and ODS F/M steels with a displacement damage less than 1.0 dpa [11,13,14]. The possible hardness contributor might be small He bubbles and small dislocation loops, although no clear examination was performed. It was shown that the F/M steels thermally aged at 600 °C [10] still maintained a hardening which was considered to be mainly due to He bubbles. To be noted, solute segregation and associated precipitation as well as clusters and dislocation loops induced by neutron irradiation might contribute to the hardening in a wide temperature range of 400–550 °C [27]. Below 250 °C, except for the direct contribution by high number density tiny He bubbles and He-vacancy complexes, additional hardenings could be induced by interstitial clusters or dislocation loops produced by punching from over-pressurized bubbles [28]. Furthermore, the dislocation loops survived during collision cascades could lead to an enhanced hardening by He-implantation, which was found in a reduced-activation martensitic steel with the He-ion implantation (580 appm/0.226 dpa) at 80–150 °C [29].

The amount of hardening was estimated by the following Orowan equation applied to expressing the short-range interaction between cavities and dislocations:

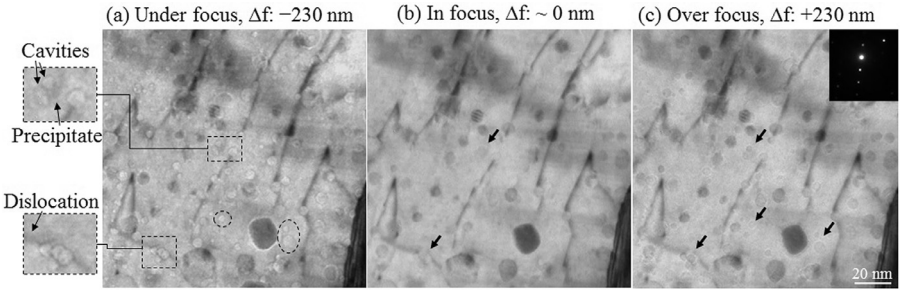

Fig. 7. Microstructures in the specimen after PIA imaged at under-focus (a); in-focus (b); over-focus (c) by using $\boldsymbol{g} = [1\bar{1}0]$ close to zone [111] with $s_g \neq 0$. Two enlarged pictures on the left end show typical nucleation sites of cavities at precipitates and dislocation. Cavities marked by dashed circles in Fig. 6(a) may be isolated. Positions for comparison were shown by arrows. The depth range: ~1000–1300 nm.

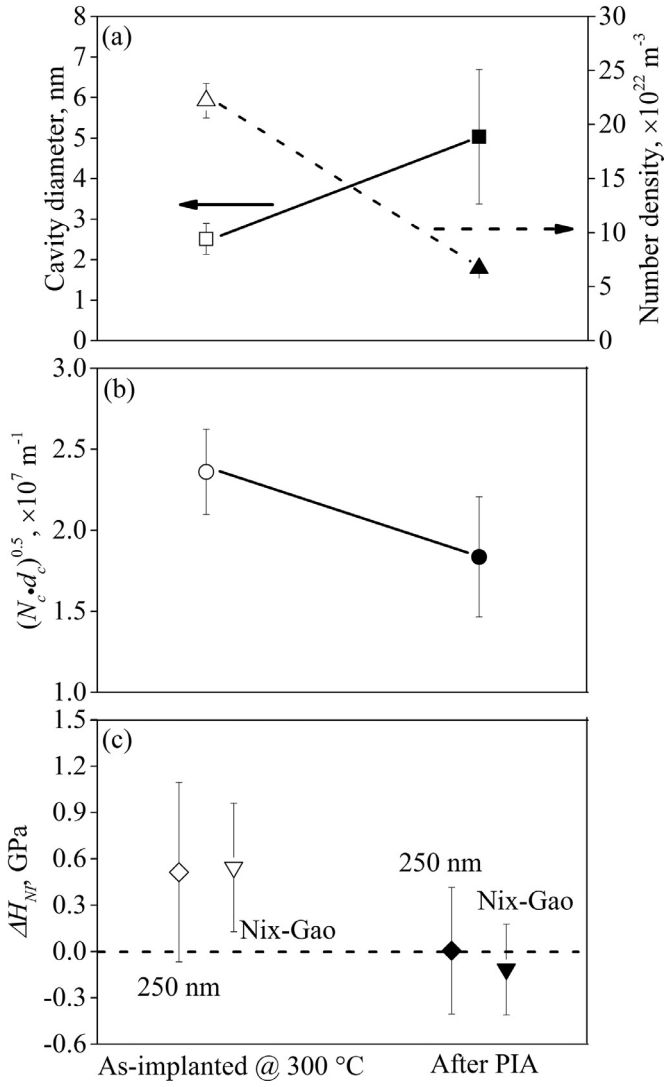

Fig. 8. (a) Diameter, d_c, number density, N_c of cavities; and (b) $(d_c \times N_c)^{0.5}$ for the as-implanted at 300 °C and the PIA; (c) The hardening before and after He-implantation at 300 °C and the hardness difference between the specimens after PIA and the un-implanted but thermally aged at 800 °C/100 h.

$$\Delta\sigma_c = M\alpha_c\mu b(N_c d_c)^{0.5} \quad (2)$$

where $\Delta\sigma_c$ is the change in the tensile yield stress; M is the Taylor factor (3.06); α_c is the barrier strength factor of cavities; μ is the shear modulus (80 GPa for alpha iron); b is the Burgers vector (0.248 nm for 1/2 < 111 > dislocations in alpha iron); N_c and d_c are the number density and mean diameter of cavities, respectively. Since the number density and the diameter of He cavities decreased and increased, respectively, after the PIA treatment, the hardness change was estimated by comparing the value, $(N_c d_c)^{0.5}$, which was reduced by the PIA. In short, the softening was induced by the PIA, as shown in Fig. 8. The increase of nanoindentation hardness can be calculated following the relationship between nanoindetantion hardness H_{NI} and yield stress σ_y: H_{NI} (MPa) = $9.8\sigma_y$ / (3.06 × 0.76) (MPa) [21]. With the obtained values of N_c and d_c of the specimens before and after He-implantation, most of the barrier strength factors were estimated to be less than 0.1, as shown in Table 1, which was almost in agreement with the value of about 0.1 for He bubbles of sizes 1–1.5 nm in neutron irradiated F/M steels [10].

4. Conclusions

15Cr-ODS ferritic steel was implanted with 3500 appm He (0.2 dpa) at 300, 550 and 700 °C. Post-implantation annealing (PIA) at 800 °C/100 h was conducted on the specimen implanted at 300 °C. Nanoindentation (NI) tests were carried out to investigate the temperature dependent hardening, and transmission electron microscopy (TEM) was performed to characterize the cavity evolution. The following main results were obtained:

1) A limited hardening was observed for the as-implanted ODS specimens at all implantation temperatures, which tended to reduce with increasing the temperature. The PIA caused no further hardening.
2) There was an evident change in the cavity distribution morphology by the PIA. The cavity diameter increased from 2.5 ± 0.4 nm to 5.0 ± 1.7 nm and the corresponding number density decreased from (22.2 ± 1.6) × 10^{22} m^{-3} to (6.7 ± 0.5) × 10^{22} m^{-3} before and after the PIA.
3) The negligible hardening accompanied by the change in the cavity morphology in the PIA treated specimen demonstrated that cavities were the weak barriers to the dislocation motion in the present ODS ferritic steel, allowing the corresponding barrier strength factor to be less than 0.1.

Acknowledgments

The first author wishes to acknowledge Japanese Government (MEXT) for scholarship and the China Scholarship Council for their kind support. The authors are also grateful to the technical support by members of Application of Duet and Muster for Industrial Research and Engineering (ADMIRE), Kyoto University.

References

[1] A. Kimura, R. Kasada, N. Iwata, H. Kishimoto, C.H. Zhang, J. Isselin, P. Dou, J.H. Lee, N. Muthukumar, T. Okuda, M. Inoue, S. Ukai, S. Ohnuki, T. Fujisawa, T.F. Abe, Development of Al added high-Cr ODS steels for fuel cladding of next generation nuclear systems, J. Nucl. Mater. 417 (2011) 176–179.
[2] G.R. Odette, M.J. Alinger, B.D. Wirth, Recent developments in irradiation-resistant steels, Annu. Rev. Mater. Res. 38 (2008) 471–503.

[3] S.J. Zinkle, L.L. Snead, Designing radiation resistance in materials for fusion energy, Annu. Rev. Mater. Res. 44 (2014) 241–267.
[4] R.J. Kurtz, A. Alamo, E. Lucon, Q. Huang, S. Jitsukawa, A. Kimura, R.L. Klueh, G.R. Odette, C. Petersen, M.A. Sokolov, P. Spätig, J.-W. Rensman, Recent progress toward development of reduced activation ferritic/martensitic steels for fusion structural applications, J. Nucl. Mater. 386–388 (2009) 411–417.
[5] P. Jung, J. Henry, J. Chen, J.-C. Brachet, Effect of implanted helium on tensile properties and hardness of 9% Cr martensitic stainless steels, J. Nucl. Mater. 318 (2003) 241–248.
[6] J. Henry, M.-H. Mathon, P. Jung, Microstructural analysis of 9% Cr martensitic steels containing 0.5 at.% helium, J. Nucl. Mater. 318 (2003) 249–259.
[7] K. Farrell, T.S. Byun, Tensile properties of ferritic/martensitic steels irradiated in HFIR, and comparison with spallation irradiation data, J. Nucl. Mater. 318 (2003) 274–282.
[8] J. Henry, X. Averty, Y. Dai, P. Lamagnère, J.P. Pizzanelli, J.J. Espinas, P. Wident, Tensile properties of 9Cr-1Mo martensitic steel irradiated with high energy protons and neutrons, J. Nucl. Mater. 318 (2003) 215–227.
[9] Y. Dai, X.J. Jia, K. Farrell, Mechanical properties of modified 9Cr-1Mo (T91) irradiated at $\leq$ 300 °C in SINQ Target-3, J. Nucl. Mater. 318 (2003) 192–199.
[10] L. Peng, Y. Dai, Helium-induced hardening effect in ferritic/martensitic steels F82H and Optimax-A irradiated in a mixed spectrum of high energy protons and spallation neutrons, J. Nucl. Mater 417 (2011) 996–1000.
[11] L. Fave, M.A. Pouchon, M. Döbeli, M. Schulte-Borchers, A. Kimura, Helium ion irradiation induced swelling and hardening in commercial and experimental ODS steels, J. Nucl. Mater. 445 (2014) 235–240.
[12] P. Song, Z. Zhang, K. Yabuuchi, A. Kimura, Helium bubble formation behavior in ODS ferritic steels with and without simultaneous addition of Al and Zr, Fusion Eng. Des. 125 (2017) 396–401.
[13] M. Roldán, P. Fernández, J. Rams, D. Jiménez-Rey, E. Materna-Morris, M. Klimenkov, Comparative study of helium effects on EU-ODS EUROFER and EUROFER97 by nanoindentation and TEM, J. Nucl. Mater. 460 (2015) 226–234.
[14] F. Bergner, G. Hlawacek, C. Heintze, Helium-ion microscopy, helium-ion irradiation and nanoindentation of Eurofer 97 and ODS Eurofer, J. Nucl. Mater. In press.
[15] P.D. Edmondson, C.M. Parish, Q. Li, M.K. Miller, Thermal stability of nanoscale helium bubbles in a 14YWT nanostructured ferritic alloy, J. Nucl. Mater. 445 (2014) 84–90.
[16] Q. Li, C.M. Parish, K.A. Powers, M.K. Miller, Helium solubility and bubble formation in a nanostructured ferritic alloy, J. Nucl. Mater 445 (2014) 165–174.
[17] A. Kohyama, Y. Katoh, M. Ando, K. Jimbo, A new Multiple Beams–Material Interaction Research Facility for radiation damage studies in fusion materials, Fusion Eng. Des. 51–52 (2000) 789–795.
[18] http://www.srim.org.
[19] R.E. Stoller, M.B. Toloczko, G.S. Was, A.G. Certain, S. Dwaraknath, F.A. Garner, On the use of SRIM for computing radiation damage exposure, Nucl. Instrum. Methods Phys. Res. Sect. B 310 (2013) 75–80.
[20] W.D. Nix, H. Gao, Indentation size effects in crystalline materials: a law for strain gradient plasticity, J. Mech. Phys. Solids 46 (1998) 411–425.
[21] R. Nakai, K. Yabuuchi, S. Nogami, A. Hasegawa, The effect of voids on the hardening of body-centered cubic Fe, J. Nucl. Mater. 471 (2016) 233–238.
[22] C.K. Dolph, D.J. da Silva, M.J. Swenson, J.P. Wharry, Plastic zone size for nanoindentation of irradiated Fe–9%Cr ODS, J. Nucl. Mater 481 (2016) 33–45.
[23] Y. Ha, A. Kimura, Effect of recrystallization on ion-irradiation hardening and microstructural changes in 15Cr-ODS steel, Nucl. Instrum. Methods Phys. Res. Sect. B 365 (2015) 313–318.
[24] R. Kasada, Y. Takayama, K. Yabuuchi, A. Kimura, A new approach to evaluate irradiation hardening of ion-irradiated ferritic alloys by nano-indentation techniques, Fusion Eng. Des. 86 (2011) 2658–2661.
[25] J. Chen, P. Jung, W. Hoffelner, H. Ullmaier, Dislocation loops and bubbles in oxide dispersion strengthened ferritic steel after helium implantation under stress, Acta Mater. 56 (2008) 250–258.
[26] R.E. Stoller, G.R. Odette, Analytical solutions for helium bubble and critical radius parameters using a hard sphere equation of state, J. Nucl. Mater. 131 (1985) 118–125.
[27] R.L. Klueh, A.T. Nelson, Ferritic/martensitic steels for next-generation reactors, J. Nucl. Mater. 371 (2007) 37–52.
[28] E.H. Lee, J.D. Hunn, G.R. Rao, R.L. Klueh, L.K. Mansur, Triple ion beam studies of radiation damage in 9Cr–2WVTa ferritic/martensitic steel for a high power spallation neutron source, J. Nucl. Mater. 271–272 (1999) 385–390.
[29] R. Kasada, T. Morimura, A. Hasegawa, A. Kimura, Effect of helium implantation on mechanical properties and microstructure evolution of reduced-activation 9Cr-2 W martensitic steel, J. Nucl. Mater. 299 (2001) 83–89.